Direct and specific assessment of axonal injury and spinal cord microenvironments using diffusion correlation imaging

Dan Benjamini[a,b,*], Elizabeth B. Hutchinson[c], Michal E. Komlosh[a,b], Courtney J. Comrie[c], Susan C. Schwerin[b,d], Guofeng Zhang[e], Carlo Pierpaoli[e], Peter J. Basser[a]

[a]*The Eunice Kennedy Shriver National Institute of Child Health and Human Development, National Institutes of Health, Bethesda, MD 20817, USA*
[b]*The Center for Neuroscience and Regenerative Medicine, Uniformed Service University of the Health Sciences, Bethesda, MD 20814, USA*
[c]*The Department of Biomedical Engineering, The University of Arizona, Tucson, Arizona 85721, USA*
[d]*Department of Anatomy, Physiology, and Genetics, Uniformed Services University of the Health Sciences, Bethesda, MD 20814, USA*
[e]*National Institute of Biomedical Imaging and Bioengineering, National Institutes of Health, Bethesda, MD 20817, USA*

Abstract

We describe a practical two-dimensional (2D) diffusion MRI framework to deliver specificity and improve sensitivity to axonal injury in the spinal cord. This approach provides intravoxel distributions of correlations of water mobilities in orthogonal directions, revealing sub-voxel diffusion components. Here we use it to investigate water diffusivities along axial and radial orientations within spinal cord specimens with confirmed, tract-specific axonal injury. First, we show using transmission electron microscopy (TEM) and immunohistochemistry that tract-specific axonal beading occurs following Wallerian degeneration in the cortico-spinal tract (CST) as direct sequelae to closed head injury (CHI). We demonstrate that although some voxel-averaged diffusion tensor imaging (DTI) metrics are sensitive to this axonal injury, they are non-specific, i.e., they do not reveal an underlying biophysical mechanism of injury. Then we employed 2D diffusion correlation imaging (DCI) to improve discrimination of different water microenvironments by measuring and mapping the joint water mobility distributions perpendicular and parallel to the spinal cord axis. We determined six distinct diffusion spectral components that differ according to their microscopic anisotropy and mobility. We further identified a distinct microenvironment that is specifically associated with the injury-induced axonal degeneration, with reduced and increased diffusivities parallel and perpendicular, respectively, hallmarks of axonal beading. An injury-specific MR image of the CHI spinal cord was then generated, and a radiological-pathological correlation with histological silver staining % area was performed. The resulting large and significant correlation ($r = 0.79$, $p < 0.0001$) indicates the high specificity with which DCI detects injury-induced tissue alterations. We predict that the ability to selectively image microstructural changes following axonal injury in the spinal cord can be useful in clinical and research applications, by enabling specific detection and increased sensitivity to injury-induced microstructural alterations. These results also encourage us to translate DCI to higher spatial dimensions to enable assessment of traumatic axonal injury, and possibly other diseases and disorders in the brain.

Keywords: DDCOSY, axonal injury, specificity, diffusion, correlation, distribution, MADCO, MRI, spectrum, Wallerian degeneration

1. Introduction

Diffusion magnetic resonance imaging (dMRI) can reveal nervous system pathology by its sensitivity to changes in the microscale tissue environment (Le Bihan et al., 1986). These measurements provide information about the translational apparent self-diffusion coefficient D, which in a complex and heterogeneous systems such as biological tissues, describes the water mobility along the particular direction in which the diffusion is encoded (Stejskal and Tanner, 1965). The most established dMRI technique, diffusion tensor imaging (DTI) (Basser et al., 1994), provides a framework for estimating the voxel-averaged macroscopic diffusivity and diffusion anisotropy in tissue, frequently expressed in terms of the mean diffusivity (MD) and the fractional anisotropy (FA), respectively.

The FA in particular has become established as a sensitive metric for detecting subtle differences in the brain tissue environment that correspond to structural features of healthy brain development (Lebel et al., 2008) and aging (Madden et al., 2012), as well as for identifying pathological alterations in disease states (Pierpaoli et al., 2001; Englund et al., 2004; Péran et al., 2010; Teipel et al., 2014). This high sensitivity of FA to cell and tissue level features owes to the integration across microstructural shape information as well as mesoscale architecture and the arrangement of cells and fiber pathways. Because such a wide range of tissue changes can affect FA and other DTI metrics, DTI is commonly proposed to detect subtle pathology that is invisible to conventional MRI, for example in diagnosing mild brain injury (Haacke et al., 2010; Shenton et al., 2012) which can be accompanied by pronounced microscale alterations – axonal varicosities or "beading", demyelination, gliosis, etc. – without overt changes in standard MRI.

*Corresponding author. Phone: +1-301-435-3868
Email address: dan.benjamini@nih.gov (Dan Benjamini)

Despite its microscopic sensitivity, models such as DTI can be non-specific, making it challenging to elucidate the origin and biological basis of cellular changes (Hutchinson et al., 2018b). Voxel-averaged metrics such as FA may particularly suffer from partial volume effects, where the signal from individual voxels frequently reflects an average of different diffusion profiles (e.g., resulting from different orientation of WM tracts or cerebrospinal fluid). This confound was shown to lead to less pronounced diffusion directionality and lower FA (Oouchi et al., 2007; Vos et al., 2011). On the other hand, complex WM architecture (e.g., crossing, kissing, fanning WM tracts) introduces a higher degree of orientation dispersion, consequently resulting in decreased FA (Pierpaoli et al., 1996; Alexander et al., 2001; Nilsson et al., 2012). Fiber architecture and voxel size may therefore greatly affect the measured DTI metrics regardless of the underlying microstructure. These competing effects can complicate the interpretation of DTI metrics except in regions of highly coherent WM (De Santis et al., 2014), which is estimated to account for less than 10% of the total white matter of the human brain (Vos et al., 2012).

Thus, conventional 1D dMRI methods, like DTI, employ single diffusion encoding (SDE) that describes water mobility in tissue along distinct directions (Stejskal and Tanner, 1965), where effects of orientation and restriction are intrinsically entangled. To be able to fully characterize a heterogeneous system, including directly measuring microscopic anisotropy, one would require to describe it using a distribution of tensors. Such a nonparametric 6D tensor distribution would embody information about the microstructural shapes, length scales, and orientations. By assuming the tensors within a voxel were distributed according to a Wishart distribution, Jian *et al.* were able to resolve complex WM intra-voxel architecture using their parametric tensor distribution model (Jian et al., 2007). Although other parametric or model-based tensor distribution estimation approaches were later suggested (Leow et al., 2009; Scherrer et al., 2016), estimating a nonparametric 6D tensor distribution, i.e., without *a priori* assuming its shape, is still a challenging task due to significant data requirements and theoretical and numerical difficulties in estimating these high-dimensional distributions.

About three decades ago a 2D dMR experiment, double diffusion encoding (DDE) NMR, where two magnetic field gradient pairs are applied consecutively (Fig. 1), was shown to be capable of disentangling the contributions of isotropic and anisotropic diffusion in the measured signal (Cory et al., 1990; Mitra, 1995). DDE can be used in conjunction with tissue models to evaluate the microscopic anisotropy (Komlosh et al., 2007; Lawrenz et al., 2010; Lawrenz and Finsterbusch, 2015), average size (Koch and Finsterbusch, 2008; Komlosh et al., 2013, 2018), size distribution (Benjamini et al., 2014, 2016; Anaby et al., 2019), and compartment eccentricity (Ozarslan, 2009; Jespersen et al., 2013; Benjamini and Basser, 2014).

Because of the ability to independently encode diffusion in different directions (Callaghan and Komlosh, 2002), DDE proved to be a natural step toward estimating a 6D tensor distribution by allowing Callaghan and Furó to reconstruct 2D projections of the 6D tensor distribution, which they termed diffusion-diffusion correlation spectroscopy (DDCOSY) nuclear magnetic resonance (NMR) (Callaghan and Furó, 2004). With this method, the DDE acquisition correlates diffusive motions along orthogonal or collinear magnetic field gradient directions. Correlations of water mobility can then be revealed by observing the 2D distribution of diffusivities along the prescribed directions without imposing a parametric structural tissue model (Qiao et al., 2005; Zong et al., 2017).

The DDCOSY NMR method was recently generalized from 2D to a 4D size-shape-orientation distribution, by imposing the constraint that all the tensors within the distribution had axial symmetry (de Almeida Martins and Topgaard, 2016), reducing the dimensionality of the 6D tensor distribution to 4D. This NMR method employed a triple diffusion encoding (TDE) to be able to capture the 4D tensor distribution, but a modified TDE sequence was suggested to reduce the computational complexity and the data requirements of the 4D tensor distribution approach by avoiding its estimation in the first place, thus allowing its integration with MR imaging. In this implementation harmonically modulated gradients along all three axes are used instead of rectangular gradients, effectively making the diffusion encoding akin to performing magic-angle spinning (MAS) about a fixed axis (Eriksson et al., 2013). This qMAS-encoded signal was shown to be independent of contributions from anisotropic diffusion, and to be sensitive mainly to the rate of isotropic diffusion, thus distinguishing between pore size and domain orientation in an indirect manner, and without actually reconstructing the tensor distribution (Lasič et al., 2014; Szczepankiewicz et al., 2015; Westin et al., 2016).

In this work we characterized and directly assessed diffusion correlations between the axial and radial axes in spinal cord specimens with confirmed and specific injury-induced axonal Wallerian degeneration (Waller, 1850; Carroll, 2009). We elected to study this well-characterized injury paradigm for which the primary morphologic features in the sub-acute period are axonal beading with some myelin damage as a means to explore the specificity of DDCOSY in a tissue environment with biologic relevance beyond phantom studies (Komlosh et al., 2017), but with less complexity than injury in brain tissue (Hutchinson et al., 2018b). Because axial symmetry and orientational coherence are reasonable assumptions to make in the spinal cord, we hypothesized that 2D projections onto the axial and radial directions of the diffusion tensor distribution could be used to assess the injury with high specificity. We used the marginal distributions constrained optimization (MADCO) framework (Benjamini and Basser, 2016) to accelerate data acquisition and obtain voxelwise DDCOSY MR images, or simply diffusion correlation imaging (DCI), of healthy and injured ferret spinal cord specimens.

2. Theory

Pfeuffer *et al.* suggested describing diffusion in heterogeneous media using a distribution of effective diffusivities by modeling the signal as a multiexponential function with respect to b and D (Pfeuffer et al., 1999). Although it was well known that Gaussian diffusion was not universally applicable

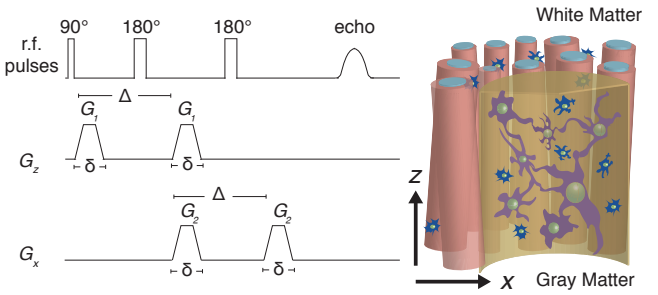

Figure 1: The DDE sequence with rapid succession of orthogonal diffusion gradient blocks.

to biological tissue, this method provided a phenomenological description of the range of water mobilities in such systems (Pfeuffer et al., 1999; Topgaard and Söderman, 2002; Yablonskiy et al., 2003; Ronen et al., 2006; Zong et al., 2017; Kim et al., 2017; Benjamini et al., 2017; Slator et al., 2019; Benjamini and Basser, 2019; Williamson et al., 2019). This approach inspired the tensor distribution model (Tuch et al., 2002), which is a generalization of the 1D multiexponential distribution.

Thus, for the 1D case the functional form of the diffusion parameters is assumed to be exponential, i.e., $K(b, D) = \exp(-bD)$, and the transformation in this case is to a domain of exponential parameters with a finite range. Such transformation, which is an example of an inverse problem, is achieved by decomposing the signal attenuation, M, into a sum of N exponential components each with unique diffusivity and probability of occurrence, $F(D)$,

$$M(b) = \sum_{n=1}^{N} F(D_n)\, K(b, D_n) + \epsilon(b), \tag{1}$$

where $\epsilon(b)$ is the experimental noise. Callaghan and Furó introduced DDCOSY and extended this framework such that a DDE acquisition with rapid succession of orthogonal diffusion gradient blocks can be used to probe the 2D diffusion correlations between those directions, as shown in Fig. 1 (Callaghan and Furó, 2004). When probing diffusion correlations in the x-z plane, Eq. 1 is generalized to

$$M(b_x, b_z) = \sum_{n_z=1}^{N_z} \sum_{n_x=1}^{N_x} F(D_{n_x}, D_{n_z}) \exp[-b_x D_{n_x} - b_z D_{n_z}] + \epsilon(b_x, b_z), \tag{2}$$

Because the functional form that relates D and b is smooth and continuous, solving the Fredholm integral in Eq. 1 is an ill-posed inverse problem (Farrar and Glauber, 1967; Epstein and Schotland, 2008), which means that the solution does not vary smoothly with the data. The main implication is that a unique and stable solution in the presence of noise does not exist. To overcome this limitation, a nearly universal approach for estimating distributions of MR parameters is to prescribe their range, and to impose nonnegativity constraints on the distributions.

Equations 1 and 2 can be expressed in vector and matrix notation by writing the distribution F as $\mathbf{f} \in \Re^{N\times 1}$ and $\mathbf{f} \in \Re^{N_x N_z \times 1}$, respectively. The multidimensional signal can be written as $\mathbf{m} \in \Re^{N_b \times 1}$, with N_b being the number of acquired data points. The kernel, K can be written as the matrix $\mathbf{K} \in \Re^{N_b \times N}$ and $\mathbf{K} \in \Re^{N_b \times N_x N_z}$, for the 1D and 2D variants, respectively. In this case, Eqs. 1 and 2 can be written in matrix form as

$$\mathbf{m} = \mathbf{K}\mathbf{f} + \epsilon, \tag{3}$$

Estimating $\mathbf{f}$ is not straightforward. The most common strategy to solve this ill-posed inverse problem is to use regularization or, alternatively, a Monte Carlo method to estimate not only one but an entire ensemble of solutions (Prange and Song, 2009; de Almeida Martins and Topgaard, 2016). Here, we chose to use ℓ_2 regularization and not the MC method because of the inherently high sensitivity of the MC method to noise in the data (Benjamini and Basser, 2020). Hence, Eq. 3 can be solved as the following regularized nonnegative least-squares minimization problem (Provencher, 1982; Kroeker and Mark Henkelman, 1986):

$$\hat{\mathbf{f}} = \arg\min_{\mathbf{f}\geq 0} (\|\mathbf{K}_0\mathbf{f} - \mathbf{m}\|_2^2 + \alpha\|\mathbf{f}\|_2^2). \tag{4}$$

The regularization term on the right hand side uses an ℓ_2 norm, called Tikhonov regularization (Tikhonov and Arsenin, 1977). Its use implicitly assumes that the system contains a continuous distribution of physical and chemical microenvironments, which has been standard practice in many previous works spanning more than three decades (Kroeker and Mark Henkelman, 1986; Menon and Allen, 1991; Fordham et al., 1995; Pfeuffer et al., 1999; Venkataramanan et al., 2002; Song et al., 2002b; MacKay et al., 2006; Ronen et al., 2006; Mitchell et al., 2012; Reiter et al., 2016; Thrane et al., 2019). Importantly, the quadratic nature of the regularization term guarantees the existence of a unique solution to Eq. 4 (Venkataramanan et al., 2002). Selecting the regularization tuning parameter, α, was done using the L-curve method (Lawson and Hanson, 1974), with the triangle algorithm for finding its corner (Castellanos et al., 2002). For further discussion regarding the choice of α, and also comparison of different inversion techniques, the reader is referred to Mitchell et al. (2012).

In addition to the commonly applied spectral constraints, i.e., nonnegativity and limited bandwidth of D, we used here the MADCO framework (Benjamini and Basser, 2014; Benjamini et al., 2016), which expands the scope of the applied spectral constraints by using the more accessible marginal distributions to enforce physical constraints on the multidimensional distribution. In our case, we can use the estimated 1D water mobility spectra in x and in z, $F(D_x)$ and $F(D_z)$, while solving Eq. 4 with the 2D data such that

$$\|\sum_{n_x=1}^{N_x} \mathbf{F}(D_{n_x}, D_{n_z}) - F(D_z)\|_2 < \sigma_z \tag{5a}$$

$$\|\sum_{n_z=1}^{N_z} \mathbf{F}(D_{n_x}, D_{n_z}) - F(D_x)\|_2 < \sigma_x, \tag{5b}$$

where σ is set according to the noise variance of the measurement. These spectral inequality constraints can be applied as a set of additional spectral constraints, thus vastly reducing the required amount of data and significantly improving the stability of the inversion process (Benjamini et al., 2016; Benjamini and Basser, 2017, 2018).

As mentioned earlier, we assume axial symmetry in this study because of the spinal cord's known neuroanatomy. In this case, $D_\perp = D_x$ and $D_\parallel = D_z$ are the radial and axial diffusivities, respectively. The computation of the FA is also reduced to

$$FA = \frac{\left|D_\parallel - D_\perp\right|}{\sqrt{D_\parallel^2 + 2D_\perp^2}}. \tag{6}$$

To facilitate the interpretation of the results we will be using $D_\perp$ and $D_\parallel$ notations from now on.

3. Materials and Methods

3.1. Specimen preparation

The animals used in this study were housed and treated at the Uniformed Services University of the Health Sciences (USUHS) according to national guidelines and institutional oversight. Perfusion fixed spinal cords were obtained from a collection of specimens taken as part of a larger study of closed head injury (CHI) in adult male ferrets (Hutchinson et al., 2018a). Two cervical cord sections were selected, one from an uninjured control and the other one-week following CHI, which resulted in focal corticospinal tract (CST) hemorrhage that was confirmed by hypointensities in *in vivo* susceptibility weighted images of the animal (Hutchinson et al., 2019). Wallerian degeneration was expected along the CST, but not along other pathways. The animals were euthanized and underwent transcardial perfusion with ice-cold 0.1 M phosphate buffered saline (PBS, pH 7.4, Quality Biological) followed by 4% paraformaldehyde (PFA, Santa Cruz Biotechnology, in PBS 0.1 M pH 7.4) at USUHS, according to standard methods. The spinal cords were then transferred to a PBS-filled container for 12 days to ensure any residual PFA was removed from the tissue. The two specimens were immersed in perfluoropolyether (Fomblin LC/8, Solvay Solexis, Italy), and inserted into the same 10 mm NMR tube (Shigemi Inc., Japan).

3.2. MRI data acquisition

MRI data were collected using a 10 mm coil with a 7T wide-bore vertical magnet and an AVANCE III MRI spectrometer equipped with a Micro2.5 microimaging probe and three GREAT60 gradient amplifiers (Bruker BioSpin, Billerica, MA), which have a nominal peak current of 60 A per channel. This configuration can produce a maximum nominal gradient strength of 24.65 mT/m/A along each of the three orthogonal directions. DCI data were acquired using a spin-echo DDE weighted echo planar imaging (DDE–EPI) sequence with diffusion encoding gradients applied in parallel (z) and perpendicular (x) to the spinal cord axis of symmetry (axial and radial, respectively), as shown in Fig. 1.

A full 2D DDCOSY acquisition requires stepping independently two successive pairs of diffusion encoding gradient pulses with orthogonal directions, $G_1 = G_z$ and $G_2 = G_x$, which is typically on the order of $32 \times 32 = 1024$ gradient steps (Callaghan and Furó, 2004; Zong et al., 2017). Here, the MADCO framework was used to reduce the number of required data points (Benjamini and Basser, 2016; Benjamini et al., 2017). Accordingly, an hierarchical sampling scheme was adopted such that first 1D diffusion data in both experimental directions is acquired by stepping G_z while G_x is held at zero, and vice versa. In this step we used 19 linearly sampled G_z that resulted in b_z-values ranging from 0 to 6700 s/mm^2 to encode diffusion in the parallel axis (i.e., D_z) and 22 linearly sampled G_x that resulted in b_x-values ranging from 0 to 36000 s/mm^2 to encode diffusion along the perpendicular axis (i.e., D_x). Two-dimensional DDE data was acquired using highly sparse encoding of 25 sampled combinations of b_z and b_x within the above 1D acquisition range. This hierarchical encoding scheme led to a total of 66 diffusion weighted images, which represents about 6.5% of the conventionally used DDCOSY data.

Other acquisition parameters were diffusion gradient duration and separation of $\delta = 3$ ms and $\Delta = 30$ ms, respectively, TR = 800 ms, and TE = 21 ms. A single 1 mm axial slice with a matrix size of 90×90 and in-plane resolution of $100 \times 100\ \mu\text{m}^2$ was acquired with 4 averages and 8 segments.

3.3. MRI data processing

One-dimensional data were first used to estimate the water mobility spectra in each image voxel by solving Eq. 4 for each diffusion encoding direction, i.e., x and z. With the 1D distributions as constraints, the 2D data sets were then processed by using the MADCO framework (Benjamini et al., 2016) to solve Eq. 4 with the 2D DDE data. All data processing was performed with in-house code written in MATLAB (The Mathworks, Natick, MA). To resolve the 2D spectra subject to the MADCO constraints we used CVX, a package for specifying and solving convex optimization problems (Grant and Boyd, 2008; CVX Research, 2012).

To evaluate the voxel-averaged $D_\perp$ and $D_\parallel$ we used a subset of the DDE dataset. For $D_\perp$, a monoexponential fit was performed with $b_z = 0$ and 4 values of b_x kept under 1000 s/mm^2. For $D_\parallel$, a monoexponential fit was performed with $b_x = 0$ and 6 values of b_z kept under 1000 s/mm^2.

3.4. Estimating variability and uncertainty

The intrinsic variability between solutions of Eq. 4 with different sampling schemes was used to quantify the uncertainty of our estimates (Prange and Song, 2009; Topgaard, 2017). We solved Eq. 4 for 100 bootstrap samples containing two thirds of the full dataset (i.e., 16 points) randomly sampled without replacement from the measured signal. This procedure results in a 100 different realizations of $P(D_\parallel, D_\perp)$ in each of the image voxels. As will be detailed in the Results section, these spectra were further processed, thus identifying and extracting significant spectral components (SC) that could then be used to reconstruct images. The variability and uncertainty of the estimated SCs could be obtained from their distribution following

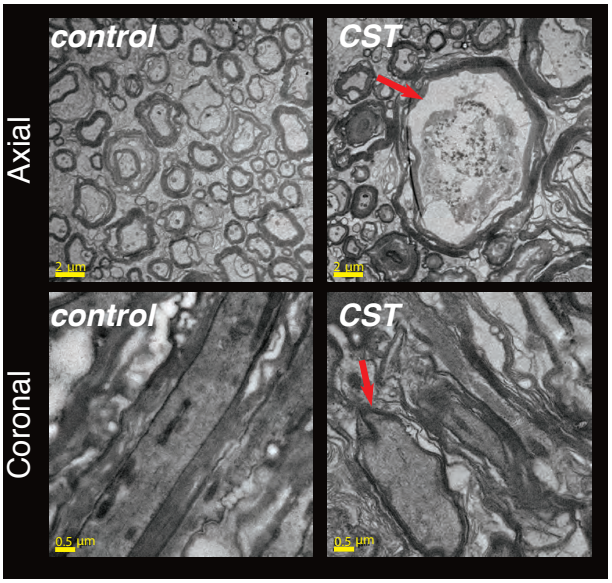

Figure 2: Electron microscopy imaging was used to validate the existence and extent of the axonal injury in the CST. Cross-sectional (axial) and longitudinal (coronal) planes were imaged, both from the control and from the TBI specimen. Local swelling of the injured region was observed, indicated by the red arrow in the axial plane. In addition, note the elongated axons in the control sample, compared with the more rounded, beaded, axons at the injury site.

the bootstrap procedure. Images of the standard deviation and of the lower and upper boundaries of the 95% confidence interval of each of the SCs are shown in the Supplementary Material.

3.5. Microscopy

3.5.1. Immunohistochemistry

Adjacent specimens of spinal cord tissue from the MRI scanned tissue were evaluated by histology analysis of neuronal and glial density, morphology and pathology. Each specimen was cut into two 10 mm lengths so that histology could be performed for both coronal and axial slices and the specimens were sent for commercial histological processing (FD Neurotechnologies, Ellicot City, MD) where they were cryoprotected, frozen and cryosectioned to 40 μm thickness. For evaluation of axonal damage, Silver staining was performed with the FD NeuroSilver Kit II (see manual PK301 at www.fdneurotechnologies.com for procedures and references). For the evaluation of axon and myelin content, double immunohistochemistry was performed using primary antibodies for myelin/oligodendrocyte glycoprotein (MOG, Sigma-Aldrich, SAB1406138) and neurofilament (NF, Enzo Life Sciences, BML-NA1297) with labeling antibodies of AlexaFluor 488 (green) and AlexaFluor 594 (red) respectively. For evaluation of astrocytes and microglia, double immunohistochemistry was performed with primary antibodies for glial fibrillary acidic protein (GFAP, abcam, ab4674) and ionized calcium-binding adaptor molecule 1 (IBA-1, Wako Chemicals USA, 019-19741) with labeling antibodies of AlexaFluor 488 (green) and AlexaFluor 594 (red) respectively. All immunofluorescent sections were co-labeled with DAPI (blue).

3.5.2. TEM

After MRI scanning, $0.5 \times 0.5 \times 1$ mm^3 cubes of tissue were cut from within the CST region of each specimen and from the uninjured dorsal column (DC) region in two orientations, axial and coronal, so that these planes could be evaluated. These sections were then fixed by newly prepared 2.0% Glutaraldehyde, 2.5% PFA in 0.1 M cacodylate buffer (pH = 7.4) for 1 hr at room temperature. Fixed samples were washed 3 times by 0.1 M cacodylate buffer and then were post-fixed in 1.0% osmium tetroxide in 0.1 M cacodylate buffer. After several washed by 0.1 M cacodylate buffer, the samples were dehydrated by incubation in the increasing concentrations of ethanol and 3 times with 100% ethanol. Samples were then infiltrated with Epon-Aradite (Ted Pella, Redding, CA): 30% Epon-Aradite in ethanol for 2 hr, 50% for 4 hr, 75% overnight, and 100% for 1 day with 2 changes. Samples were polymerized at 60°C for 2 days. Ultrathin sections (about 80 nm) were cut with a Reichert Ultracut E Microtome and collected on copper slot grids. Sections were counter-stained with uranyl acetate and lead citrate, and examined under a FEI Tecnai12 transmission electron microscope operating with a beam energy of 120 keV. Images were acquired using a Gatan 2k×2k cooled CCD camera.

3.5.3. Image processing

Whole-slice images were collected using digital slide scanning microscopy at 20x magnification, such that 1 pixel = 0.32×0.32 μm^2. For silver stained sections, optical imaging was performed using a Nanozoomer system (Hamamatsu Photonics, Hamamatsu, Japan) and for florescence imaging, a Zeiss Axio Scan Z1 system was used (Carl Zeiss Microscopy, Thornwood, NY, United States). All images were exported in TIFF format for offline processing.

The color balance tool on ImageJ was used on both the fluorescent and silver stained images. For qualitative analysis, the fluorescent stained image was further split into separate RGB channels, and then the red and green channels were recombined.

The % area of silver staining was quantified after binarization of the grayscale image using a locally adaptive threshold procedure (Bradley and Roth, 2007), thus avoiding the need to manually selecting a threshold value.

3.6. Histology-MRI co-registration

Following convergence of 2D affine co-registration of histology and MR images (Image Processing Toolbox, MATLAB, The Mathworks, Natick, MA), we performed 2D diffeomorphic registration refinement between the silver stained image slices and MRI volumes. This was done in order to recover true in-plane tissue shape and bridge over residual differences between the modalities. The diffeomorphic registration procedure in this paper was performed using an efficient implementation of the greedy diffeomorphic algorithm (Joshi et al., 2004), provided as an open-source software package that was *greedy*[1] modeled after Symmetric Normalization (SyN) in the ANTS software

[1] `greedy` codebase: `https://github.com/pyushkevich/greedy`.

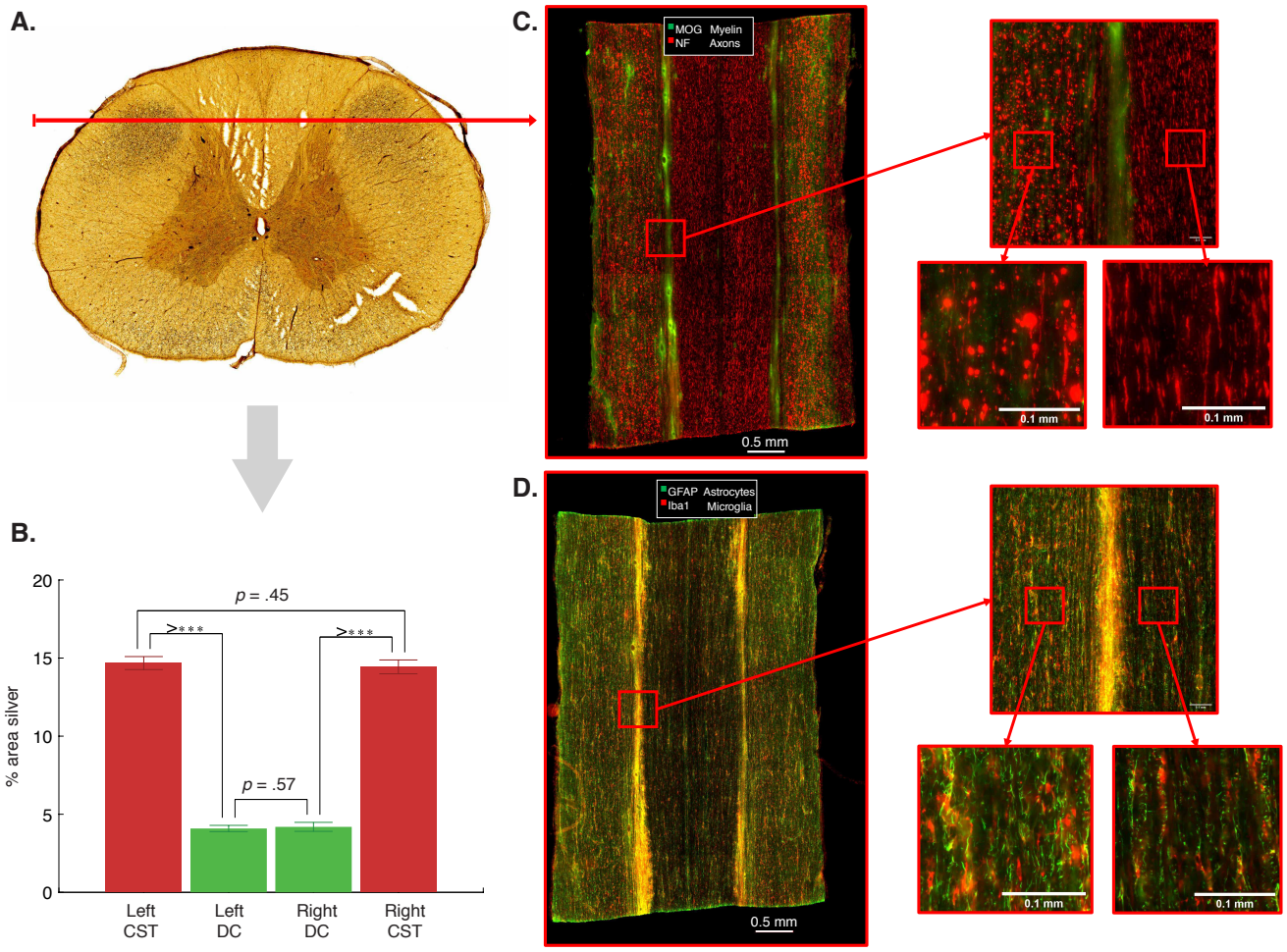

Figure 3: Confirmation of tract-specific injury. (A) Prominent positive silver staining in the CST of the injured spinal cord. (B) Quantitative comparisons of % area of silver staining between left and right CST and DC regions. A two-sample t-test determined that CST had significantly higher value of % area of silver staining than the DC region, and that the injury was symmetric in both left and right CSTs. Three asterisks signify that $p \leq .001$. (C) IHC images of NF and MOG showing axonal beading and demyelination processes limited to the CST. (D) Glia IHC revealed modest increases in astrocyte reactivity and microglial density.

package (Avants et al., 2008). Our implementation is optimized for computational speed, foregoing the symmetric registration model and implementing a highly optimized image resampling and metric computation. The *greedy* software was initialized and used as previously described (Adler et al., 2018).

4. Results

4.1. Confirmation and characterization of tract-specific injury

Tract-specific axonal injury was independently confirmed by histopathology and TEM of the spinal cord specimens. Transmission electron microscopy images showed large axonal varicosities or beads in both the axial and coronal planes at the injured CST region when compared with uninjured regions or the control specimen (Fig. 2).

Positive silver staining was prominent in the CST of the injured spinal cord and not in the adjacent DC region or in any tract of the control specimen (Fig. 3A). Quantitative comparisons of % area of silver staining between left and right CST and DC regions were performed by using four 500×500 pixel ROIs from the thresholded image in each of the damaged (CST) and control (DC) regions. The resulting values in the CST were 14.7 ± 0.4 (left) and 14.4 ± 0.4 (right), as compared with the DC at 4.1 ± 0.2 (left) and 4.2 ± 0.3 (right). A two-sample t-test was done on pairs of these ROIs, which determined that CST had significantly higher value of % area of silver staining than the DC region, and that the injury was symmetric in both left and right ROIs (Fig. 3B).

More specific evaluation using immunohistochemistry (IHC) showed severe beading by NFL staining as well as MOG positive detritus consistent with demyelinating processes in the CST but not in other regions (Fig. 3C). Astrocyte IHC showed modest increases in GFAP staining, but not prominent enough to suggest severe reactivity of astrocytes (Fig. 3D). Microglial staining by Iba-1 revealed a modest increase in microglial density, especially of microglia having a phagocytic morphology. This profile is highly consistent with Wallerian degeneration and by and large, the greatest alteration appeared to be axonal damage, especially beading. Taken together with the TEM results, these demonstrate tract-specificity of damage in the in-

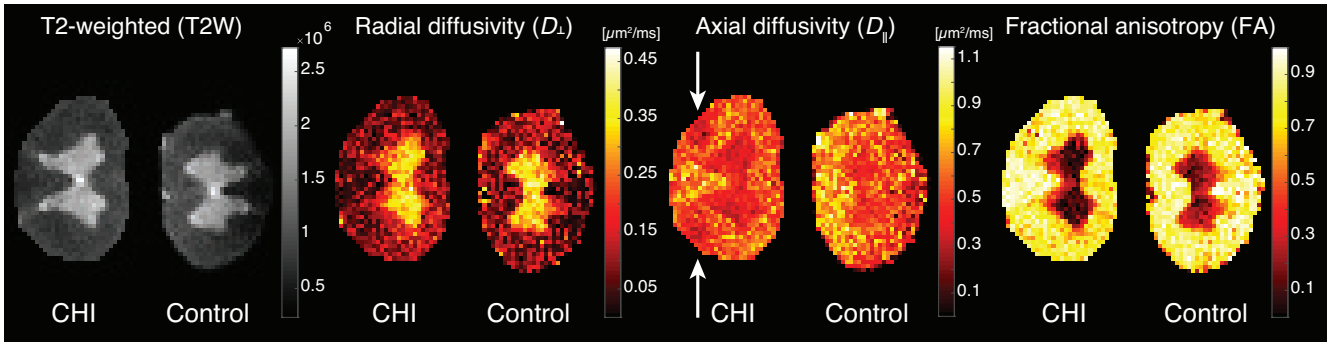

Figure 4: Voxel-averaged MRI. From left to right, T2W, $D_\perp$, $D_\parallel$, and FA images. Note the insensitivity of the T2W and $D_\perp$ images to the axonal injury in the CST region of the left hand side spinal cord. Slight hypointensity in the $D_\parallel$ image is evident at the injury site (white arrows), although it is non-specific to the axonal injury and is seen in the GM as well.

jured specimen and axonal morphology as the most prominent microscale correlate of pathology in the injured tract.

4.2. *Voxel-averaged MR images are sensitive but non-specific to axonal injury*

Voxel-averaged scalar images can only provide macroscopic information with respect to the voxel size, which in most cases will contains multiple chemical and physical water pools or microenvironments. The basic DTI metrics, $D_\perp$, $D_\parallel$, and FA, are all examples of voxel-averaged quantities that are known for their relatively high microstructural sensitivity. These images, along with a T2-weighted (T2W) image of the spinal cords, are shown in Fig. 4. No apparent abnormalities were observed in the T2W, $D_\perp$, and FA images; these did not show any sensitivity to axonal injury. Compared with adjacent WM, a moderate drop in $D_\parallel$ at the CST of the injured specimen was observed (indicated with white arrows). However, GM voxels exhibited low $D_\parallel$ values as well, illustrating how this DTI metric is sensitive to axonal injury, yet is non-specific.

A more formal statistical analysis of these observations is summarized in Fig. 5. Three ROIs in the injured specimen – GM, WM, and the CST (their location shown in Fig. 7) – were selected for comparisons. For each of the DTI metrics, a two-sample t-test was done on all pairs of ROIs to determine whether they are significantly different from one another. The axial diffusivity was the only metric to significantly drop from normal WM (0.54 ± 0.01 $\mu m^2/ms$) to injured WM in the CST (0.42 ± 0.01 $\mu m^2/ms$). However, $D_\parallel$ was not able to distinguish between GM (0.43 ± 0.01 $\mu m^2/ms$) and injured CST WM, pointing to lack of specificity. With both the $D_\perp$ and FA metrics, the only significant differences were observed between GM and WM, regardless whether it was injured or normal.

4.3. *Distinct $D_\perp - D_\parallel$ correlation spectral components*

Instead of assuming that each voxel contains a scalar value, we propose here a phenomenological description to the 2D DDE signal that provides the 2D distribution of water mobility in x and z, in our case, the axial and radial directions, respectively. Each voxel contains these distributions, and the first

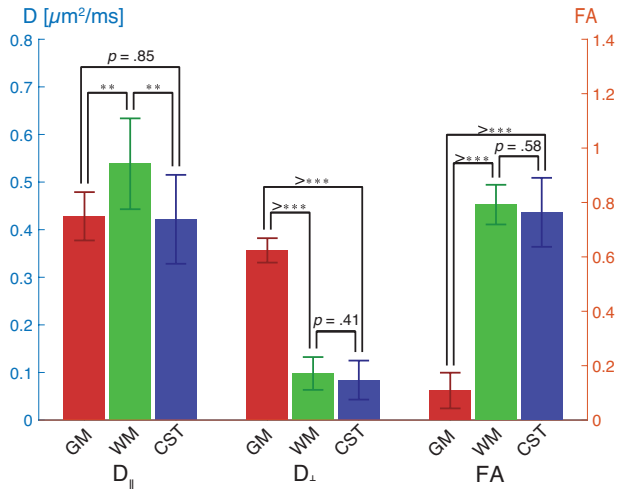

Figure 5: Regions of interest statistical analysis of voxel-averaged DTI metrics from the injured spinal cord. A two-sample t-test was done on all pairs of ROIs – GM, normal WM, and CST – to determine whether they are significantly different from one another. The $D_\parallel$ metric was sensitive to microstructural alterations in the injury site, however, was non-specific. Two and three asterisks signify that $p \leq .01$ and $p \leq .001$, respectively.

step in studying this system is to define spectral regions of interest (sROI), i.e., regions that contain distinct components in the axial-radial mobility spectra.

It is impractical to manually examine single voxels to determine the sROIs. Instead, in most multidimensional MRI studies an average spectrum across the entire image domain is computed, and used to manually assign sROIs (Kim et al., 2017; Slator et al., 2019). Although simple to implement, this approach may lead to loss of important spectral information due to spatial averaging. Particularly true in our case, a spectral component (SC) that is unique to the axonal injury would be limited to a small number of CST voxels, and will most likely be averaged-out if a simple average were used. Instead, we used a recently proposed method that preserves inter-voxel variability by giving equal weight to all SCs in each voxel across the image (Pas et al., 2020). The resulting summarized radial-axial diffusion correlation distributions from the CHI and control spinal cords are shown in Figs. 6A and B, respectively. The red di-

agonal line marks where the axial and radial diffusivities are equal, and thus, where diffusion is completely isotropic.

The two spectra in Figs. 6A and B appear to be quite similar, and in fact, as confirmed by microscopy, the axonal injury is tract-specific, and therefore, most of the CHI sample should appear to be normal. To identify the sROIs we used a two-steps method: (1) Using the summarized 2D spectra we first applied the sROI generator algorithm proposed in (Pas et al., 2020) separately on the two spinal cords to obtain rectangular sROIs. This process resulted in 5 distinct components (1–5) in both CHI and control specimens, and a 6th component that was identified only in the injured spinal cord. (2) We then manually refined these rectangular sROIs to arbitrary shapes (sROIs 1–6 in Fig. 6) to improve the resulting spatial maps. When examining such correlation spectra it is useful to keep in mind that the farther the SCs are from the diagonal, the more microscopically anisotropic the microenvironment from which they originate is. Similarly, the farther the SCs are from the origin, the higher the water mobility is.

Although our data allows for a voxelwise analysis, it is prudent to first perform an ROI analysis. The same ROIs as before were chosen, namely, GM, normal WM, and CST, in both the CHI and control sample, and their corresponding axial-radial diffusion correlation spectra are shown in Fig. 7. The first observations are that WM and GM present unique and distinguishable spectral features, and that the spectra from these normal regions in both control and TBI specimens were similar, which strengthens the validity of this comparative study.

As expected, in both control and CHI samples $P(D_\perp, D_\parallel)$ of GM contained mainly microscopically isotropic components, with most of the spectral intensity concentrated in sROIs 1 and 2 (Fig. 7A). Conversely, $P(D_\perp, D_\parallel)$ in normal WM predominantly contained two populations with moderate and high degree of microscopic anisotropy in sROIs 4 and 5, respectively (Fig. 7B). Lastly, the axial-radial diffusion correlation in the CST ROI was examined. The control CST spectrum (Fig. 7C, bottom) was very similar, as expected, to the other normal WM spectra (Fig. 7B), with SCs at the same sROIs. Compared with normal WM, $P(D_\perp, D_\parallel)$ at the injury site had a very noticeable change: the highly anisotropic component (SC 5) had shifted towards the diagonal line to sROI 6, and became more microscopically isotropic (Fig. 7C, top). The increased microscopic isotropy at the injury site might reflect axonal beading that has occurred.

4.4. *Diffusion correlation components capture axonal injury with high specificity*

Generating images from multidimensional spectra requires dimensionality reduction to achieve a more compact representation of the spectral information. The most commonly used strategy in this context is to compute the relative signal fractions of the SCs in each voxel and display them as images (Mackay et al., 1994; Labadie et al., 1994), which is achieved by summing (i.e., numerically integrating) over the predefined sROIs.

Signal fraction images of the 6 different $P(D_\perp, D_\parallel)$ components are shown in Fig. 8. Corresponding micro-tensors along

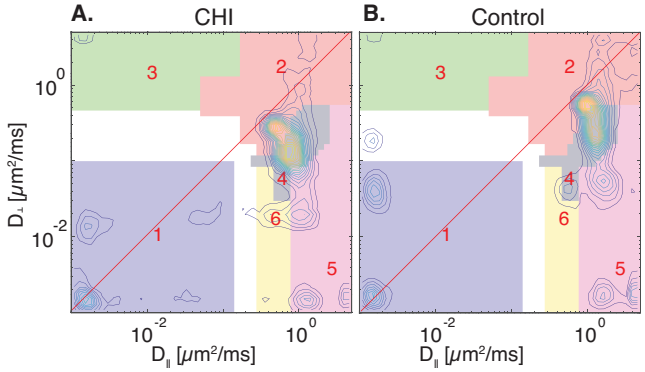

Figure 6: Summarized diffusion correlation spectra of the (A) CHI and (B) control specimens. These spectra were computed using a framework for processing and image reconstruction of multidimensional correlation MRI data (Pas et al., 2020). Spectral ROIs (1 – 6) were determined using these summarized spectra, and are shown with different colors.

with their microscopic FA, μFA (under axial symmetry and orientational coherence assumptions), are shown above the SCs images. The μFA values were computed by plugging median values of $D_\perp$ and $D_\parallel$ from each sROI in Eq. 6. The median values of $D_\perp$, $D_\parallel$, and μFA from each sROI are summarized in Table 1. The interquartile range (IQR) is used to capture the spread of the logarithmically spaced data, with the first and third quartiles as the lower and upper bounds, respectively.

Two microscopically isotropic SCs, 1 and 2, were identified, with μFA of 0.10 and 0.33, respectively. While SC 1, which is mainly limited to WM, was characterized by very low water mobility, SC 2 has shown relatively high water mobility and is mainly restricted to GM. Component 3 is anisotropic, oriented perpendicular to the spinal cord axial plane. Spatially, this SC is only present in the GM and in low intensity, and is postulated to originate from root fibers that run in-plane.

Components 4 and 5 both exhibited anisotropic diffusion oriented along the z plane. While both were mainly observed in the WM, SC 4 was characterized by a significantly lower μFA due to increased $D_\perp$ and reduced $D_\parallel$, compared with SC 5 (Table 1). In addition, SC 5 provided a clear boundary of the axonal injury area (Fig. 8), where this highly microscopically anisotropic diffusion could no longer exist, possibly due to beading of the injured axons.

The last spectral peak, SC 6, had larger $D_\perp$ than SC 5, and a markedly reduced $D_\parallel$ compared with both SCs 4 and 5 (Table 1). The spatial map of SC 6 clearly shows a very specific pattern, with hyper-intensities that are limited to the CST of the injured spinal cord (Fig. 8).

We quantified the uncertainty of the SCs estimates using a bootstrap procedure that yielded 100 realizations of the diffusion correlation spectra (described in more detail in the Materials and Methods section). Distributions of SCs in each voxel were then obtained by applying the same sROIs on all $P(D_\parallel, D_\perp)$ realizations. The average value of the standard deviations of these distributions across all SCs and voxels was 0.0102 ± 0.0096. Bearing in mind that SC values range from 0 to 1, and compared with the average value across all SCs and

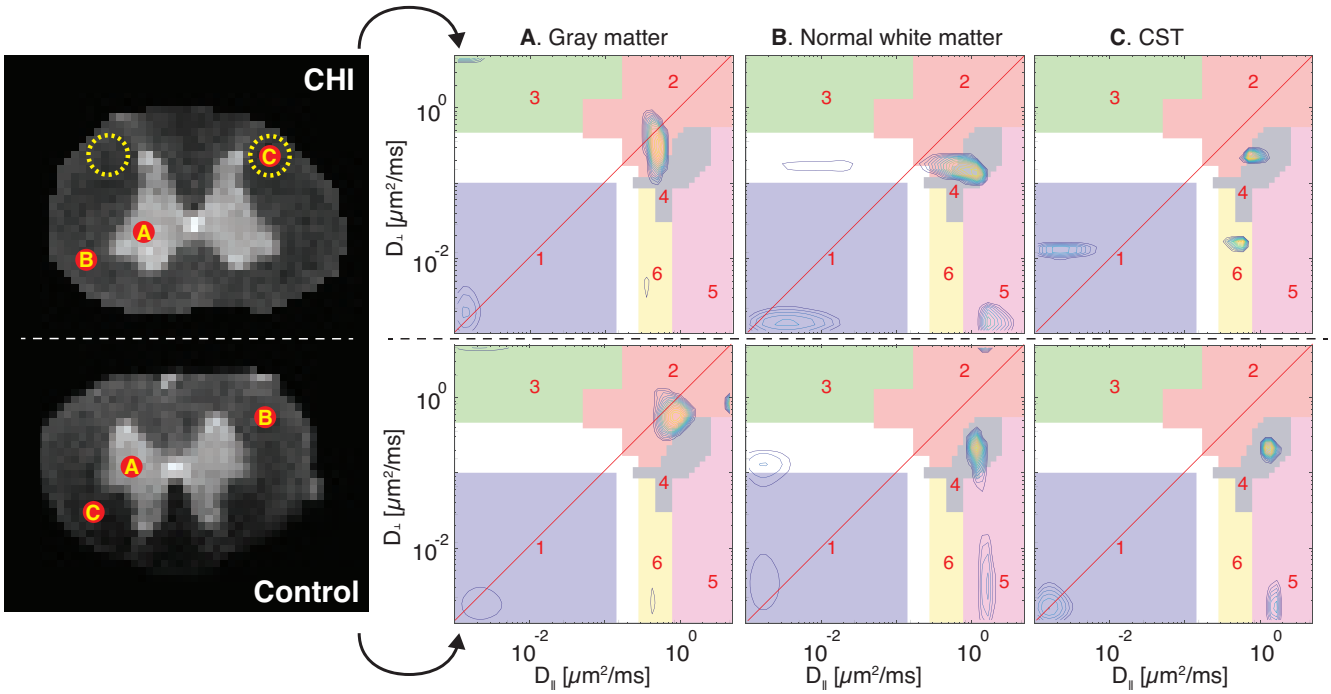

Figure 7: Regions of interest analysis of the two specimens. Three ROIs were chosen: (A) GM, (B) normal WM, and (C) the CST (injury site). Control and CHI diffusion correlation spectra from these ROIs are shown, respectively, in the bottom and top panels. Both ROIs A and B have similar SCs in all of the sROIs, suggesting that the injury is indeed localized and not systemic. The CST spectra of the control and CHI spinal cords are markedly different: a highly anisotropic component in sROI 5 is present in both control and CHI ROI B, and in control ROI C, while it is clearly absent in the CST of the CHI sample. Further, the same highly anisotropic component has shifted to sROI 6 as a result of the axonal injury, and is now characterized by much more microscopically isotropic diffusion.

voxels of 0.1563 ± 0.1670, the uncertainty of the estimated SCs is quite low. Images of the SC standard deviation and of the lower and upper boundaries of the 95% confidence interval are shown in Figs. S1 and S2, respectively, in the Supplementary Material.

To determine whether DCI could potentially used to assess axonal injury in the spinal cord, we performed radiological-pathological correlation analyses on multiple ROIs with histological silver staining % area and diffusion correlation SCs 5 and 6. Twenty ROIs, mainly in the CST and DC, in the co-registered injured spinal cord images were selected (Fig. 9A). We found that silver staining % area and SCs 5 and 6 were significantly correlated ($r = -0.68$, $p < 0.001$, and $r = 0.79$, $p < 0.0001$, respectively), as seen in Figs. 9B and C, respectively. The strong correlations indicate the high specificity of these components to the traumatic brain injury (TBI)-induced beading.

5. Discussion

In summary, we found that specific 2D SCs obtained from DCI are highly correlated with corresponding histology in a spinal cord specimen with tract-specific axonal beading following Wallerian degeneration. Conversely, DTI metrics did not show any significant specificity to identify the injury.

We confirmed by both TEM and immunohistochemical histology that cellular alterations in our specimen corresponded with injury-induced axonal degeneration in the sub-acute period. Furthermore, this pathology was limited to the CST and not found in other tracts of the same specimen or in a control specimen. Direct comparison of the injured and control specimens demonstrated robustness and reproducibility of the DCI metrics in unaffected tracts and showed significant and prominent differences selectively in the injured tract.

We have identified a diffusion component (SC 6) with reduced $D_{\parallel}$ and increased $D_{\perp}$ compared with normal WM. This reduction in μFA was caused by decreased and elevated water mobility in the axial and radial directions, respectively. Such changes in the observed diffusion characteristics is consistent with the expected microstructural alterations following axonal beading. The corresponding signal fraction of the beaded population was about 0.1, and was strongly correlated with silver staining % area.

Changes in the voxel-averaged radial diffusivity were expected based on previous *ex vivo* spinal cord studies (Zhang et al., 2009), and on our TEM and histological data, however, it was completely insensitive to the injury. Moreover, previous studies have demonstrated that myelin damage can result in an increase in radial diffusivity in myelinated white matter (Gulani et al., 2001; Song et al., 2002a), and indeed, MOG immunohistochemistry in this study indicated limited demyelination at the injury site. The insensitivity of the measured voxel-average $D_{\perp}$ in the affected tract could arise from the observed low degree of myelin damage and glial reactivity, in addition to the partial volume effects from averaging over the voxel.

Decrease in DTI-derived axial diffusivity is one of the first

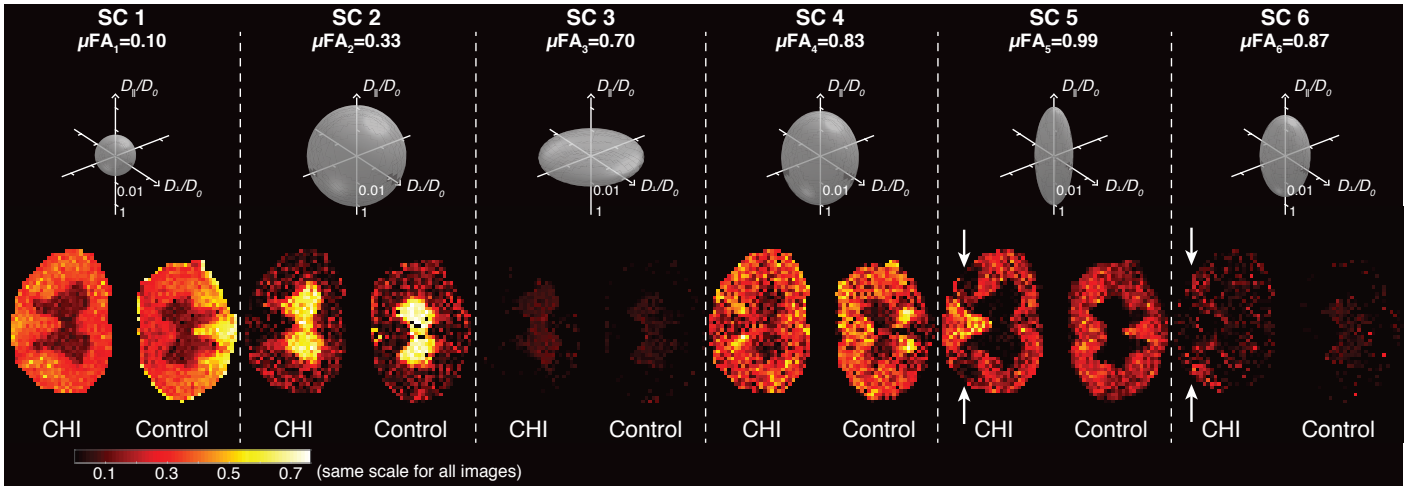

Figure 8: Generated images of the distinct microscopic water mobility regimes. Image intensities reflect the signal fraction of specific diffusion components in the corresponding sROI. Above each image is an axisymmetric microscopic diffusion tensor ellipsoid that depicts the water mobility regime of each component (assuming domain orientational coherence), along with its μFA. Note that the micro-tensor diffusivity values are plotted on a logarithmic scale normalized by D_0=2 μm^2/ms. In the context of this axonal injury, the most informative diffusion correlation SCs were 5 and 6. Component 5 provided a clear boundary of the injury area, where this highly microscopically anisotropic diffusion is no longer possible. Instead, injured axons can be directly observed by looking at SC 6, which is described by a significantly more microscopically isotropic diffusion behavior.

imaging signatures associated with axonal injury (Beaulieu et al., 1996; Mac Donald et al., 2007; Zhang et al., 2009; Budde et al., 2009). The voxel-averaged axial diffusivity in our study was the only DTI metric that appeared to be sensitive to injury, where a reduced value compared with normal WM was observed. The most likely cellular underpinning of this reduction is greater hinderance of axial diffusion due to the presence of axonal varicosities. Despite that, this metric was not able to distinguish between injured and GM regions, and therefore was shown to be non-specific to axonal beading.

The ROI analysis showed that although the voxel-average FA drop at the CST compared with normal WM, the reduction was not statistically significant. This result was expected because it is directly linked to the insensitivity of the voxel-average $D_\perp$, which dominates the calculation of the FA (Eq. 6).

Apart from the abnormal water mobility in the CST, we identified 5 unique diffusion microenvironments. The first, SC1, is a microscopically isotropic population with very low mobility that was observed in all regions of the spinal cord, with increased intensities in WM (average signal fractions across both spinal cord specimens of 0.35 ± 0.10 and 0.15 ± 0.09 in WM and GM, respectively). A subpopulation of water molecules with very slow and isotropic diffusion in the brain was observed and explicitly modeled in previous studies (Kroenke et al., 2005; Alexander et al., 2010; Dhital et al., 2018; Tax et al., 2020). Generally, these studies reported lower fractions of low mobility water in WM than the values we found here, however, they were all performed *in vivo* and with clinical MRI scanners using considerably lower b-values and low spatial resolution that is prone to partial volume effects. In addition, none of these studies examined the spinal cord. A strong presence of a low mobility water pool in the *ex vivo* spinal cord was previously reported, with increased intensity in the dorsal WM (Benjamini et al., 2016), in agreement with the current SC1 image. Our

Table 1: Median values of $D_\perp$, $D_\parallel$, and μFA from each sROI. The interquartile range (IQR) is displayed to capture the spread of the logarithmically spaced data, with the first and third quartiles as the lower and upper bounds, respectively.

SC	$D_\perp$ (IQR) [μm^2/ms]	$D_\parallel$ (IQR) [μm^2/ms]	μFA
1	.009 (.003 – .032)	.011 (.003 – .038)	.10
2	1.05 (.621 – 2.49)	.522 (.260 – 1.48)	.33
3	1.76 (1.05 – 2.97)	.009 (.003 – .032)	.70
4	.155 (.092 – .260)	1.05 (.621 – 1.48)	.83
5	.014 (.003 – .054)	2.49 (1.48 – 3.53)	.99
6	.042 (.030 – .060)	.369 (.310 – .439)	.87

findings reaffirm previous observations that this apparent immobile water subpopulation is indeed isotropic, at least under the axial symmetry assumption. The biological interpretation of SC1 is still debatable; it was suggested that it originates from water molecules trapped in glial cells or water bound to membranes (Stanisz et al., 1997; Alexander et al., 2010; Williamson et al., 2019). Further examination and histological correlation is necessary to make a more certain determination.

We found that normal WM is mainly comprised of two anisotropic populations with ascending μFA (SCs 4 and 5, respectively). Because we used a 2D DDE acquisition that requires the assumption of fiber orientational coherence we cannot determine whether the difference between SCs 4 and 5 arises from orientational dispersion or size (or both). In GM we found two dominant diffusion correlation components: a microscopically isotropic population with moderate mobility (SC 2), and a microscopically anisotropic component oriented perpendicular to the spinal cord axial plane (SC 3), which is considered to originate from root fibers that run in-plane.

The two spinal cord specimens were placed facing each other in order to validate the assumption of axial symmetry made in this study. In this way encoding in the laboratory x direction results in diffusion being encoded in opposite directions with respect to each specimen, i.e., x is left in one sample, and right in the other sample. Showing that $P(D_\perp, D_\parallel)$ had similar characteristics in uninjured regions of both specimens despite investigating opposite directions about the spinal cord axis increases the validity of the axial symmetry assumption.

Data inversion methods used to obtain 1- and 2-D distributions of diffusivities assume that the data attenuates exponentially with b. Strictly speaking, this is only valid for a particular range of the signal attenuation, and water populations that experience ideal restricted diffusion, e.g., trapped in impermeable spheres, will appear to attenuate multiexponentially, and thus result in distributed components when inverted. In this case, although only one compartment with a single size exists (i.e., the sphere), a range of diffusion microenvironments can be used to describe this system, with apparent diffusivities that increase with the distance from the barrier or surface. Indeed, if the traditional microstructural description of biological tissue as comprised of "compartments" is avoided, different water mobility, and as a result, different diffusivity, is expected within a single "compartment".

Integration of this multidimensional approach within MR imaging applications was not feasible until recently due to burdensome data requirements causing impractically long scan times. However, here we use the MADCO framework Benjamini et al. (2016) and apply it to DDCOSY to significantly reduce data requirements, requiring only 6.5% of the spectral data as compared with previous applications (Callaghan and Furó, 2004; Zong et al., 2017), making voxelwise DCI feasible. Despite the significant improvement, DCI still requires considerably more data than DTI, which may be a reasonable penalty in return for the demonstrated high tissue components specificity.

While the underlying microstructure of neuronal tissue may be unknown and ill-defined, interpretation and biophysical modeling of diffusion processes in those systems is an active and ongoing area of research (Stanisz et al., 1997; Sen and Basser, 2005; Özarslan et al., 2013; Jelescu et al., 2016; Benjamini et al., 2016; Novikov et al., 2018; Veraart et al., 2019; Lampinen et al., 2019). Nevertheless, modeling the diffusion signal as a distribution of apparent diffusivities in neuronal tissue was shown here to effectively separate water components based on the range and orientational bias of their apparent mobilities. Nevertheless, we should interpret these spectral peaks conservatively, not viewing them as arising from individual biological compartments (e.g., intracellular vs extracellular), cell types or cell sizes.

In this 2D implementation of DCI we have shown it can be used to directly and specifically assess axonal injury in the spinal cord, where the assumption of orientational coherence is reasonable and appears to be satisfied. However, with the exception of areas in the Central Nervous System (CNS) such as the splenium and genu of the corpus callosum, optic tracts, etc., such a high degree of orientational coherence is uncommon in most brain regions. Estimating the 4D size-shape-orientation distribution would help address this issue by taking into account the fiber orientation dispersion as well. Our findings demonstrated that diffusion correlations are sensitive and specific to the morphology of axonal injury, and should serve as motivation for further research that would advance the 4D diffusion correlation NMR method (de Almeida Martins and Topgaard, 2016) towards MRI applications to assess axonal injury.

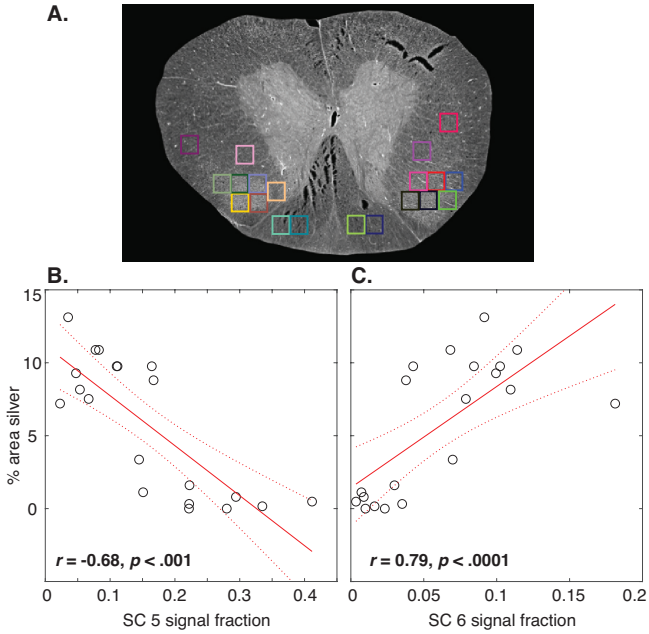

Figure 9: Silver staining % area and the corresponding diffusion correlation SCs 5 and 6. (A) The silver staining image after co-registration to the injured spinal cord MRI image. Twenty ROIs are displayed and were used for to compute individual data points in (B) and (C). (B) SC 5 had a negative correlation with silver staining % area ($r = -0.68$, $p < 0.001$). (C) SC 6 had a positive correlation with silver staining % area ($r = 0.79$, $p < 0.0001$).

6. Conclusions

This study demonstrates the feasibility of identifying and directly mapping axonal injury during the process of degeneration in the spinal cord using 2D diffusion correlation imaging (DCI). The spectroscopic results suggest that conventional maps of voxel-averaged DTI-derived metrics are subject to partial volume effects, rendering them non-specific to this type of morphologic change. By contrast, our analysis identifies multiple intravoxel diffusion components or water pools in different lying in different orientations, enabling us to reveal and directly quantify sub-voxel microscopically anisotropic components.

Using DCI we were able to isolate a diffusion correlation spectral component that was specifically associated with injury-induced axonal degeneration. The measured water mobility of that specific component was hindered in the parallel direction and increased perpendicular to it, which are the anticipated hallmarks of axonal beading. The tract-specific injury was confirmed using TEM and histopathology, the latter shown to be strongly correlated with the injury-specific MR image.

We predict that this new ability to selectively image microstructural changes following axonal injury in the spinal cord has potential for future research and clinical applications, by providing increased specificity and sensitivity to TBI-induced microstructural alterations. These results serve as an impetus to generalize this imaging method approach to higher dimensions to enable the assessment of TBI-induced axonal injury in the brain by developing intrinsic, invariant measures of axonal beading.

Acknowledgements

This work was supported by funds provided by the Intramural Research Program (IRP) of the *Eunice Kennedy Shriver* National Institute of Child Health and Human Development (grant number ZIAHD000266) and the Center for Neuroregenerative Medicine (CNRM) under the auspices of the Henry Jackson Foundation (HJF).

References

Adler, D.H., Wisse, L.E.M., Ittyerah, R., Pluta, J.B., Ding, S.L., Xie, L., Wang, J., Kadivar, S., Robinson, J.L., Schuck, T., Trojanowski, J.Q., Grossman, M., Detre, J.A., Elliott, M.A., Toledo, J.B., Liu, W., Pickup, S., Miller, M.I., Das, S.R., Wolk, D.A., Yushkevich, P.A., 2018. Characterizing the human hippocampus in aging and Alzheimer's disease using a computational atlas derived from ex vivo MRI and histology. Proceedings of the National Academy of Sciences 115, 4252–4257.

Alexander, A.L., Hasan, K.M., Lazar, M., Tsuruda, J.S., Parker, D.L., 2001. Analysis of partial volume effects in diffusion-tensor MRI. Magnetic Resonance in Medicine 45, 770–780.

Alexander, D.C., Hubbard, P.L., Hall, M.G., Moore, E.A., Ptito, M., Parker, G.J.M., Dyrby, T.B., 2010. Orientationally invariant indices of axon diameter and density from diffusion MRI. NeuroImage 52, 1374–1389.

Anaby, D., Morozov, D., Seroussi, I., Hametner, S., Sochen, N., Cohen, Y., 2019. Single- and double-Diffusion encoding MRI for studying ex vivo apparent axon diameter distribution in spinal cord white matter. NMR in Biomedicine 32.

Avants, B., Epstein, C., Grossman, M., Gee, J., 2008. Symmetric diffeomorphic image registration with cross-correlation: Evaluating automated labeling of elderly and neurodegenerative brain. Medical Image Analysis 12, 26–41.

Basser, P.J., Mattiello, J., LeBihan, D., 1994. MR diffusion tensor spectroscopy and imaging. Biophysical Journal 66, 259–67.

Beaulieu, C., Does, M.D., Snyder, R.E., Allen, P.S., 1996. Changes in water diffusion due to Wallerian degeneration in peripheral nerve. Magnetic Resonance in Medicine 36, 627–631.

Benjamini, D., Basser, P.J., 2014. Joint radius-length distribution as a measure of anisotropic pore eccentricity: An experimental and analytical framework. The Journal of Chemical Physics 141, 214202.

Benjamini, D., Basser, P.J., 2016. Use of marginal distributions constrained optimization (MADCO) for accelerated 2D MRI relaxometry and diffusometry. Journal of Magnetic Resonance 271, 40–45.

Benjamini, D., Basser, P.J., 2017. Magnetic resonance microdynamic imaging reveals distinct tissue microenvironments. NeuroImage 163, 183–196.

Benjamini, D., Basser, P.J., 2018. Towards clinically feasible relaxation-diffusion correlation MRI using MADCO. Microporous and Mesoporous Materials 269, 93–96.

Benjamini, D., Basser, P.J., 2019. Water mobility spectral imaging of the spinal cord: Parametrization of model-free Laplace MRI. Magnetic Resonance Imaging 56, 187–193.

Benjamini, D., Basser, P.J., 2020. Multidimensional correlation MRI. NMR in Biomedicine , e4226.doi:10.1002/nbm.4226.

Benjamini, D., Elsner, J.J., Zilberman, M., Nevo, U., 2014. Pore size distribution of bioresorbable films using a 3-D diffusion NMR method. Acta Biomaterialia 10, 2762–2768.

Benjamini, D., Komlosh, M.E., Basser, P.J., 2017. Imaging Local Diffusive Dynamics Using Diffusion Exchange Spectroscopy MRI. Physical Review Letters 118, 158003.

Benjamini, D., Komlosh, M.E.M., Holtzclaw, L.A.L., Nevo, U., Basser, P., 2016. White matter microstructure from nonparametric axon diameter distribution mapping. NeuroImage 135, 333–344.

Bradley, D., Roth, G., 2007. Adaptive Thresholding using the Integral Image. Journal of Graphics Tools 12, 13–21.

Budde, M.D., Xie, M., Cross, A.H., Song, S.K., 2009. Axial Diffusivity Is the Primary Correlate of Axonal Injury in the Experimental Autoimmune Encephalomyelitis Spinal Cord: A Quantitative Pixelwise Analysis. Journal of Neuroscience 29, 2805–2813.

Callaghan, P.T., Furó, I., 2004. Diffusion-diffusion correlation and exchange as a signature for local order and dynamics. The Journal of Chemical Physics 120, 4032.

Callaghan, P.T., Komlosh, M.E., 2002. Locally anisotropic motion in a macroscopically isotropic system: displacement correlations measured using double pulsed gradient spin-echo NMR. Magnetic Resonance in Chemistry 40, S15–S19.

Carroll, S., 2009. Wallerian Degeneration, in: Squire, L.R. (Ed.), Encyclopedia of Neuroscience. Academic Press, San Diego, CA, pp. 485–491.

Castellanos, J., Gómez, S., Guerra, V., 2002. The triangle method for finding the corner of the L-curve. Applied Numerical Mathematics 43, 359–373.

Cory, D., Garroway, A., Miller, J., 1990. Applications of spin transport as a probe of local geometry. Polym. Preprints 31, 149–150.

CVX Research, 2012. CVX: Matlab Software for Disciplined Convex Programming, version 2.0. URL: http://cvxr.com/cvx.

de Almeida Martins, J.P., Topgaard, D., 2016. Two-Dimensional Correlation of Isotropic and Directional Diffusion Using NMR. Physical Review Letters 116, 087601.

De Santis, S., Drakesmith, M., Bells, S., Assaf, Y., Jones, D.K., 2014. Why diffusion tensor MRI does well only some of the time: Variance and covariance of white matter tissue microstructure attributes in the living human brain. NeuroImage 89, 35–44.

Dhital, B., Kellner, E., Kiselev, V.G., Reisert, M., 2018. The absence of restricted water pool in brain white matter. NeuroImage 182, 398–406.

Englund, E., Sjobeck, M., Brockstedt, S., Latt, J., Larsson, E.M., 2004. Diffusion tensor MRI post mortem demonstrated cerebral white matter pathology. Journal of Neurology 251, 350–352.

Epstein, C.L., Schotland, J., 2008. The Bad Truth about Laplace's Transform. SIAM Review 50, 504–520.

Eriksson, S., Lasic, S., Topgaard, D., 2013. Isotropic diffusion weighting in PGSE NMR by magic-angle spinning of the q-vector. Journal of Magnetic Resonance 226, 13–18.

Farrar, D.E., Glauber, R.R., 1967. Multicollinearity in regression analysis: the problem revisited. The Review of Economics and Statistics 49, 92–107.

Fordham, E., Sezginer, A., Hall, L., 1995. Imaging Multiexponential Relaxation in the (y, LogeT1) Plane, with Application to Clay Filtration in Rock Cores. Journal of Magnetic Resonance, Series A 113, 139–150.

Grant, M.C., Boyd, S.P., 2008. Graph Implementations for Nonsmooth Convex Programs, in: Recent Advances in Learning and Control. Springer London, London, pp. 95–110.

Gulani, V., Webb, A., Duncan, I., Lauterbur, P., 2001. Apparent diffusion tensor measurements in myelin-deficient rat spinal cords. Magnetic Resonance in Medicine 45, 191–195.

Haacke, E.M., Duhaime, A.C., Gean, A.D., Riedy, G., Wintermark, M., Mukherjee, P., Brody, D.L., DeGraba, T., Duncan, T.D., Elovic, E., Hurley, R., Latour, L., Smirniotopoulos, J.G., Smith, D.H., 2010. Common data elements in radiologic imaging of traumatic brain injury. Journal of Magnetic Resonance Imaging 32, 516–543.

Hutchinson, E., Benjamini, D., Basser, P., Pierpaoli, P., Komlosh, M., 2019. Improvements in specificity by non-Gaussian diffusion modeling and double diffusion encoding (DDE) to characterize axonal injury, in: International Society for Magnetic Resonance in Medicine, Montreal, Canada.

Hutchinson, E., King, S., Kim, Y., Krotcov, A., Bosomtwi, A., Reyes, L., Schwerin, S., Juliano, S., Dardzinski, B., Pierpaoli, C., 2018a. MRI markers of brain injury in a ferret model of closed head rotation and acceleration, in: Society for Neuroscience, San Diego, CA.

Hutchinson, E.B., Schwerin, S.C., Avram, A.V., Juliano, S.L., Pierpaoli, C., 2018b. Diffusion MRI and the detection of alterations following traumatic brain injury. Journal of Neuroscience Research 96, 612–625.

Jelescu, I.O., Veraart, J., Fieremans, E., Novikov, D.S., 2016. Degeneracy in model parameter estimation for multi-compartmental diffusion in neuronal tissue. NMR in Biomedicine 29, 33–47.

Jespersen, S.N., Lundell, H., Sonderby, C.K., Dyrby, T.B., 2013. Orientationally invariant metrics of apparent compartment eccentricity from double pulsed field gradient diffusion experiments. NMR in Biomedicine 26, 1647–1662.

Jian, B., Vemuri, B.C., Özarslan, E., Carney, P.R., Mareci, T.H., 2007. A novel tensor distribution model for the diffusion-weighted MR signal. NeuroImage 37, 164–176.

Joshi, S., Davis, B., Jomier, M., Gerig, G., 2004. Unbiased diffeomorphic atlas construction for computational anatomy. NeuroImage 23, S151–S160.

Kim, D., Doyle, E.K., Wisnowski, J.L., Kim, J.H., Haldar, J.P., 2017. Diffusion-relaxation correlation spectroscopic imaging: A multidimensional approach for probing microstructure. Magnetic Resonance in Medicine 78, 2236–2249.

Koch, M.A., Finsterbusch, J., 2008. Compartment size estimation with double wave vector diffusion-weighted imaging. Magnetic Resonance in Medicine 60, 90–101.

Komlosh, M., Benjamini, D., Barnett, A., Schram, V., Horkay, F., Avram, A., Basser, P., 2017. Anisotropic phantom to calibrate high-q diffusion MRI methods. Journal of Magnetic Resonance 275, 19–28.

Komlosh, M.E., Benjamini, D., Hutchinson, E.B., King, S., Haber, M., Avram, A.V., Holtzclaw, L.A., Desai, A., Pierpaoli, C., Basser, P.J., 2018. Using double pulsed-field gradient MRI to study tissue microstructure in traumatic

brain injury (TBI). Microporous and Mesoporous Materials 269, 156–159.
Komlosh, M.E., Horkay, F., Freidlin, R.Z., Nevo, U., Assaf, Y., Basser, P.J., 2007. Detection of microscopic anisotropy in gray matter and in a novel tissue phantom using double Pulsed Gradient Spin Echo MR. Journal of Magnetic Resonance 189, 38–45.
Komlosh, M.E., Özarslan, E., Lizak, M.J., Horkayne-Szakaly, I., Freidlin, R.Z., Horkay, F., Basser, P.J., 2013. Mapping average axon diameters in porcine spinal cord white matter and rat corpus callosum using d-PFG MRI. NeuroImage 78, 210–6.
Kroeker, R.M., Mark Henkelman, R., 1986. Analysis of biological NMR relaxation data with continuous distributions of relaxation times. Journal of Magnetic Resonance (1969) 69, 218–235.
Kroenke, C.D., Bretthorst, G.L., Inder, T.E., Neil, J.J., 2005. Diffusion MR imaging characteristics of the developing primate brain. NeuroImage 25, 1205–1213.
Labadie, C., Lee, J., Vetek, G., Springer, C., 1994. Relaxographic Imaging. Journal of Magnetic Resonance, Series B 105, 99–112.
Lampinen, B., Szczepankiewicz, F., Novén, M., Westen, D., Hansson, O., Englund, E., Mårtensson, J., Westin, C., Nilsson, M., 2019. Searching for the neurite density with diffusion MRI: Challenges for biophysical modeling. Human Brain Mapping 40, 2529–2545.
Lasič, S., Szczepankiewicz, F., Eriksson, S., Nilsson, M., Topgaard, D., 2014. Microanisotropy imaging: quantification of microscopic diffusion anisotropy and orientational order parameter by diffusion MRI with magic-angle spinning of the q-vector. Frontiers in Physics 2.
Lawrenz, M., Finsterbusch, J., 2015. Mapping measures of microscopic diffusion anisotropy in human brain white matter in vivo with double-wave-vector diffusion-weighted imaging. Magnetic Resonance in Medicine 73, 773–783.
Lawrenz, M., Koch, M.A., Finsterbusch, J., 2010. A tensor model and measures of microscopic anisotropy for double-wave-vector diffusion-weighting experiments with long mixing times. Journal of Magnetic Resonance 202, 43–56.
Lawson, C.L., Hanson, R.J., 1974. Solving least squares problems. Prentice-Hall, Englewood Cliffs, NJ.
Le Bihan, D., Breton, E., Lallemand, D., Grenier, P., Cabanis, E., Laval-Jeantet, M., 1986. MR imaging of intravoxel incoherent motions: application to diffusion and perfusion in neurologic disorders. Radiology 161, 401–7.
Lebel, C., Walker, L., Leemans, A., Phillips, L., Beaulieu, C., 2008. Microstructural maturation of the human brain from childhood to adulthood. NeuroImage 40, 1044–1055.
Leow, A.D., Zhu, S., Zhan, L., McMahon, K., de Zubicaray, G.I., Meredith, M., Wright, M.J., Toga, A.W., Thompson, P.M., 2009. The tensor distribution function. Magnetic Resonance in Medicine 61, 205–214.
Mac Donald, C.L., Dikranian, K., Bayly, P., Holtzman, D., Brody, D., 2007. Diffusion Tensor Imaging Reliably Detects Experimental Traumatic Axonal Injury and Indicates Approximate Time of Injury. Journal of Neuroscience 27, 11869–11876.
MacKay, A., Laule, C., Vavasour, I., Bjarnason, T., Kolind, S., Mädler, B., 2006. Insights into brain microstructure from the T2 distribution. Magnetic Resonance Imaging 24, 515–525.
Mackay, A., Whittall, K., Adler, J., Li, D., Paty, D., Graeb, D., 1994. In vivo visualization of myelin water in brain by magnetic resonance. Magnetic Resonance in Medicine 31, 673–677.
Madden, D.J., Bennett, I.J., Burzynska, A., Potter, G.G., Chen, N.k., Song, A.W., 2012. Diffusion tensor imaging of cerebral white matter integrity in cognitive aging. Biochimica et Biophysica Acta (BBA) - Molecular Basis of Disease 1822, 386–400.
Menon, R.S., Allen, P.S., 1991. Application of continuous relaxation time distributions to the fitting of data from model systmes and excised tissue. Magnetic Resonance in Medicine 20, 214–227.
Mitchell, J., Chandrasekera, T.C., Gladden, L.F., 2012. Numerical estimation of relaxation and diffusion distributions in two dimensions. Progress in Nuclear Magnetic Resonance Spectroscopy 64, 34–50.
Mitra, P., 1995. Multiple wave-vector extensions of the NMR pulsed-field-gradient spin-echo diffusion measurement. Physical Review B 51, 15074–15078.
Nilsson, M., Lätt, J., Ståhlberg, F., Westen, D., Hagslätt, H., 2012. The importance of axonal undulation in diffusion MR measurements: a Monte Carlo simulation study. NMR in Biomedicine 25, 795–805.
Novikov, D.S., Kiselev, V.G., Jespersen, S.N., 2018. On modeling. Magnetic Resonance in Medicine 79, 3172–3193.
Oouchi, H., Yamada, K., Sakai, K., Kizu, O., Kubota, T., Ito, H., Nishimura, T., 2007. Diffusion Anisotropy Measurement of Brain White Matter Is Affected by Voxel Size: Underestimation Occurs in Areas with Crossing Fibers. American Journal of Neuroradiology 28, 1102–1106.
Ozarslan, E., 2009. Compartment shape anisotropy (CSA) revealed by double pulsed field gradient MR. Journal of Magnetic Resonance 199, 56–67.
Özarslan, E., Koay, C.G., Shepherd, T.M., Komlosh, M.E., Irfanoğlu, M.O., Pierpaoli, C., Basser, P.J., 2013. Mean apparent propagator (MAP) MRI: A novel diffusion imaging method for mapping tissue microstructure. NeuroImage 78, 16–32.
Pas, K., Komlosh, M.E., Perl, D.P., Basser, P.J., Benjamini, D., 2020. Retaining information from multidimensional correlation MRI using a spectral regions of interest generator. Scientific Reports 10, 3246.
Péran, P., Cherubini, A., Assogna, F., Piras, F., Quattrocchi, C., Peppe, A., Celsis, P., Rascol, O., Démonet, J.F., Stefani, A., Pierantozzi, M., Pontieri, F.E., Caltagirone, C., Spalletta, G., Sabatini, U., 2010. Magnetic resonance imaging markers of Parkinson's disease nigrostriatal signature. Brain 133, 3423–3433.
Pfeuffer, J., Provencher, S.W., Gruetter, R., 1999. Water diffusion in rat brain in vivo as detected at very large b values is multicompartmental. Magma 8, 98–108.
Pierpaoli, C., Barnett, A., Pajevic, S., Chen, R., Penix, L., Virta, A., Basser, P., 2001. Water Diffusion Changes in Wallerian Degeneration and Their Dependence on White Matter Architecture. NeuroImage 13, 1174–1185.
Pierpaoli, C., Jezzard, P., Basser, P.J., Barnett, A., Di Chiro, G., 1996. Diffusion tensor MR imaging of the human brain. Radiology 201, 637–648.
Prange, M., Song, Y.Q., 2009. Quantifying uncertainty in NMR T2 spectra using Monte Carlo inversion. Journal of Magnetic Resonance 196, 54–60.
Provencher, S.W., 1982. A constrained regularization method for inverting data represented by linear algebraic or integral equations. Computer Physics Communications 27, 213–227.
Qiao, Y., Galvosas, P., Callaghan, P., 2005. Diffusion Correlation NMR Spectroscopic Study of Anisotropic Diffusion of Water in Plant Tissues. Biophysical Journal 89, 2899–2905.
Reiter, D.A., Magin, R.L., Li, W., Trujillo, J.J., Pilar Velasco, M., Spencer, R.G., 2016. Anomalous T 2 relaxation in normal and degraded cartilage. Magnetic Resonance in Medicine 76, 953–962.
Ronen, I., Moeller, S., Ugurbil, K., Kim, D.S., 2006. Analysis of the distribution of diffusion coefficients in cat brain at 9.4 T using the inverse Laplace transformation. Magnetic Resonance Imaging 24, 61–68.
Scherrer, B., Schwartzman, A., Taquet, M., Sahin, M., Prabhu, S.P., Warfield, S.K., 2016. Characterizing brain tissue by assessment of the distribution of anisotropic microstructural environments in diffusion-compartment imaging (DIAMOND). Magnetic Resonance in Medicine 76, 963–977.
Sen, P.N., Basser, P.J., 2005. A Model for Diffusion in White Matter in the Brain. Biophysical Journal 89, 2927–2938.
Shenton, M.E., Hamoda, H.M., Schneiderman, J.S., Bouix, S., Pasternak, O., Rathi, Y., Vu, M.A., Purohit, M.P., Helmer, K., Koerte, I., Lin, A.P., Westin, C.F., Kikinis, R., Kubicki, M., Stern, R.A., Zafonte, R., 2012. A review of magnetic resonance imaging and diffusion tensor imaging findings in mild traumatic brain injury. Brain Imaging and Behavior 6, 137–192.
Slator, P.J., Hutter, J., Palombo, M., Jackson, L.H., Ho, A., Panagiotaki, E., Chappell, L.C., Rutherford, M.A., Hajnal, J.V., Alexander, D.C., 2019. Combined diffusion-relaxometry MRI to identify dysfunction in the human placenta. Magnetic Resonance in Medicine 82, 95–106.
Song, S.K., Sun, S.W., Ramsbottom, M.J., Chang, C., Russell, J., Cross, A.H., 2002a. Dysmyelination Revealed through MRI as Increased Radial (but Unchanged Axial) Diffusion of Water. NeuroImage 17, 1429–1436.
Song, Y.Q., Venkataramanan, L., Hürlimann, M., Flaum, M., Frulla, P., Straley, C., 2002b. T1-T2 Correlation Spectra Obtained Using a Fast Two-Dimensional Laplace Inversion. Journal of Magnetic Resonance 154, 261–268.
Stanisz, G.J., Szafer, A., Wright, G.A., Henkelman, R.M., 1997. An analytical model of restricted diffusion in bovine optic nerve. Magnetic Resonance in Medicine 37, 103–111.
Stejskal, E., Tanner, J., 1965. Spin diffusion measurements: Spin echoes in the presence of a time-dependent field gradient. Journal of Chemical Physics 42, 288–292.
Szczepankiewicz, F., Lasič, S., van Westen, D., Sundgren, P.C., Englund, E., Westin, C.F.F., Ståhlberg, F., Lätt, J., Topgaard, D., Nilsson, M., Lasic, S.,

van Westen, D., Sundgren, P.C., Englund, E., Westin, C.F.F., Stahlberg, F., Latt, J., Topgaard, D., Nilsson, M., Ståhlberg, F., Lätt, J., Topgaard, D., Nilsson, M., 2015. Quantification of microscopic diffusion anisotropy disentangles effects of orientation dispersion from microstructure: Applications in healthy volunteers and in brain tumors. NeuroImage 104, 241–252.

Tax, C.M., Szczepankiewicz, F., Nilsson, M., Jones, D.K., 2020. The dot-compartment revealed? Diffusion MRI with ultra-strong gradients and spherical tensor encoding in the living human brain. NeuroImage , 116534.

Teipel, S.J., Grothe, M.J., Filippi, M., Fellgiebel, A., Dyrba, M., Frisoni, G.B., Meindl, T., Bokde, A.L., Hampel, H., Klöppel, S., Hauenstein, K., 2014. Fractional Anisotropy Changes in Alzheimer's Disease Depend on the Underlying Fiber Tract Architecture: A Multiparametric DTI Study using Joint Independent Component Analysis. Journal of Alzheimer's Disease 41, 69–83.

Thrane, L.W., Seymour, J.D., Codd, S.L., 2019. Probing diffusion dynamics during hydrate formation by high field NMR relaxometry and diffusometry. Journal of Magnetic Resonance 303, 7–16.

Tikhonov, A., Arsenin, V., 1977. Solutions of Ill-Posed Problems. Winston, New York.

Topgaard, D., 2017. Multidimensional diffusion MRI. Journal of Magnetic Resonance 275, 98–113.

Topgaard, D., Söderman, O., 2002. Self-Diffusion in Two- and Three-Dimensional Powders of Anisotropic Domains: An NMR Study of the Diffusion of Water in Cellulose and Starch. The Journal of Physical Chemistry B 106, 11887–11892.

Tuch, D.S., Reese, T.G., Wiegell, M.R., Makris, N., Belliveau, J.W., Wedeen, V.J., 2002. High angular resolution diffusion imaging reveals intravoxel white matter fiber heterogeneity. Magnetic Resonance in Medicine 48, 577–582.

Venkataramanan, L., Yi-Qiao Song, Hurlimann, M., 2002. Solving Fredholm integrals of the first kind with tensor product structure in 2 and 2.5 dimensions. IEEE Transactions on Signal Processing 50, 1017–1026.

Veraart, J., Fieremans, E., Novikov, D.S., 2019. On the scaling behavior of water diffusion in human brain white matter. NeuroImage 185, 379–387.

Vos, S.B., Jones, D.K., Jeurissen, B., Viergever, M.A., Leemans, A., 2012. The influence of complex white matter architecture on the mean diffusivity in diffusion tensor MRI of the human brain. NeuroImage 59, 2208–2216.

Vos, S.B., Jones, D.K., Viergever, M.A., Leemans, A., 2011. Partial volume effect as a hidden covariate in DTI analyses. NeuroImage 55, 1566–1576.

Waller, A.V., 1850. XX. Experiments on the section of the glossopharyngeal and hypoglossal nerves of the frog, and observations of the alterations produced thereby in the structure of their primitive fibres. Philosophical Transactions of the Royal Society of London 140, 423–429.

Westin, C.F., Knutsson, H., Pasternak, O., Szczepankiewicz, F., Özarslan, E., van Westen, D., Mattisson, C., Bogren, M., O'Donnell, L.J., Kubicki, M., Topgaard, D., Nilsson, M., 2016. Q-space trajectory imaging for multidimensional diffusion MRI of the human brain. NeuroImage 135, 345–362.

Williamson, N.H., Ravin, R., Benjamini, D., Merkle, H., Falgairolle, M., O'Donovan, M.J., Blivis, D., Ide, D., Cai, T.X., Ghorashi, N.S., Bai, R., Basser, P.J., 2019. Magnetic resonance measurements of cellular and subcellular membrane structures in live and fixed neural tissue. eLife 8, e51101.

Yablonskiy, D.A., Bretthorst, G.L., Ackerman, J.J., 2003. Statistical model for diffusion attenuated MR signal. Magnetic Resonance in Medicine 50, 664–669.

Zhang, J., Jones, M., DeBoy, C.A., Reich, D.S., Farrell, J.A.D., Hoffman, P.N., Griffin, J.W., Sheikh, K.A., Miller, M.I., Mori, S., Calabresi, P.A., 2009. Diffusion Tensor Magnetic Resonance Imaging of Wallerian Degeneration in Rat Spinal Cord after Dorsal Root Axotomy. Journal of Neuroscience 29, 3160–3171.

Zong, F., Ancelet, L.R., Hermans, I.F., Galvosas, P., 2017. Determining mean fractional anisotropy using DDCOSY: preliminary results in biological tissues. Magnetic Resonance in Chemistry 55, 498–507.